BNL-211550-2019-JAAM

An Oxygen Vacancy-rich Semiconductor Supported Bifunctional Catalyst for Efficient and Stable Zinc-Air Battery

G. Liu, D. Su

To be published in "Advanced Materials"

February 2019

Center for Functional Nanomaterials

Brookhaven National Laboratory

U.S. Department of Energy

USDOE Office of Science (SC), Basic Energy Sciences (BES) (SC-22)

DISCLAIMER

Oxygen Vacancy-rich Semiconductor Supported Bifunctional Catalyst for Efficient and Stable Zinc-Air Battery

Guihua Liu, Jingde Li, Jing Fu, Gaopeng Jiang, Gregory Lui, Dan Luo, Ya-Ping Deng, Jing Zhang, Zachary P. Cano, Aiping Yu, Dong Su, Zhengyu Bai, Lin Yang and Zhongwei Chen**

G. Liu, Dr. J. Li, Dr. J. Fu, Dr. G. Jiang, G. Lui, D. Luo, Y-P. Deng, J. Zhang, Z. P. Cano, Prof. A. Yu, Prof. Z. Chen
Department of Chemical Engineering, Waterloo Institute for Nanotechnology, Waterloo Institute for Sustainable Energy, University of Waterloo, Waterloo, Ontario N2L 3G1, Canada
E-mail: zhwchen@uwaterloo.ca

Prof. Z. Bai, Prof. L. Yang
School of Chemistry and Chemical Engineering, Key Laboratory of Green Chemical Media and Reactions, Ministry of Education, Henan Normal University, Xinxiang, 453007, China
E-mail: baizhengyu@htu.cn

Dr. D. Su
Center for Functional Nanomaterials, Brookhaven National Laboratory, Upton, NY 11953, USA

Keywords: oxygen vacancy; metal-support interaction; oxygen evolution reaction; bifunctional catalyst; zinc-air battery

Abstract

The highly oxidative operating condition of rechargeable zinc-air batteries causes significant carbon-support corrosion of bifunctional oxygen electrocatalysts. Here, we propose a new strategy for the catalyst support design focusing on OV-rich, low-bandgap semiconductor. The OVs promote the electrical conductivity of the oxide support, and at the same time offer a strong metal-support interaction (SMSI), which enables the catalysts small metal size, high catalytic activity, and high stability. The strategy is demonstrated by successfully synthesizing ultrafine Co metal decorated three-dimensionally ordered macroporous titanium oxynitride (3DOM-Co@TiO_xN_y). The 3DOM-Co@TiO_xN_y catalyst exhibits comparable activities for oxygen reduction and evolution reactions, but much higher cycling stability than noble-metals in alkaline conditions. The zinc-air battery using this catalyst delivers an excellent stability

with less than 1% energy efficiency loss over 900 charge-discharge cycles at 20 mA cm^{-2}. The high stability is attributed to the strong SMSI between Co and 3DOM-TiO_xN_y which verified by density functional theory (DFT) calculations. This work sheds light on using OV-rich semiconductors as a promising support to design efficient and durable non-precious electrocatalysts.

The practical application of rechargeable zinc-air batteries requires a low-cost, efficient and stable air electrode catalyst toward both the oxygen reduction reaction (ORR) and oxygen evolution reaction (OER). The most promising non-precious bifunctional catalysts are carbon-supported transition metal hybrid materials.[1] However, carbon-supported catalysts suffer from carbon electrochemical oxidation, which causes the loss or aggregation of supported catalysts and degrades the electrocatalysis durability and performance.[2] To alleviate this problem, some strategies have been reported including coating the carbon support with corrosion-resistive TiO_2,[3] using conductive TiN as an alternative support,[4] or developing perovskite oxides as active catalysts.[5] However, both TiO_2 and perovskite oxides have an intrinsic low-conductivity drawback, and nor TiN is an optimum support material to obtain highly dispersed and active catalysts due to the non-defective surface structure. Thus, the objective of this study is to develop a conductive and oxidation-resistant support to relieve catalyst degradation, and at the same time achieve a high bifunctional catalytic activity with enhanced durability performance.

Here, we propose that OV-rich, low-bandgap oxide semiconductor can be a promising support to design active and durable ultrafine metal catalysts in electrocatalysis (**Figure 1**a). This argument is built on our multidisciplinary understanding of OVs in semiconductor physics and heterogeneous solid-gas catalysis: *i)* the OVs lower the bandgap in oxide semiconductors: the higher OVs concentration, the higher conductivity of the oxides; [6] *ii)* in solid-gas catalysis, the OVs on oxide supports would provide a SMSI with the supported metal catalysts, and results in high metal dispersion, small metal size, high relative catalytic activity and high stability.[7] That is, the OVs are not only beneficial for the conductivity of the oxides, but it also offers a SMSI that favors the formation and stabilization of highly active ultrafine metal nanoparticles. Note that, in electrocatalysis, the role of OVs in metal oxides as active components is well reported for contributing to its enhanced catalytic activities. [8] However, the significance of OVs in supporting materials is much less discussed, in particular for processes involving the oxidative OER reaction. To the best of our knowledge, this is the first time that the concept of OVs-induced SMSI is introduced to design active and stable semiconductor-based electrocatalysts with ultrafine dispersion of the active phase for ORR and OER.

In this work, we developed an efficient and durable bifunctional catalyst which comprises OV-rich 3DOM TiO_xN_y supported ultrafine Co (Figure 1b), referred to as 3DOM-Co@TiO_xN_y. It was prepared by thermal treating polystyrene (PS) template soaked with cobalt acetate [$Co(CH_3COO)_2{\cdot}4H_2O$] and titanium butoxide [$Ti(OBu)_4$] precursor solution with an atomic ratio of Co:Ti=1:20 (Figure S1, S2). At different heating stages, Ar and NH_3 atmosphere were used. This ensures an oxygen-deficient and reductive environment that are beneficial for OVs formation in the TiO_xN_y support. Detailed synthesis procedures can be found in Supporting Information. It should be mentioned that the calcination of PS beads not only forms the 3DOM morphology, but also generates an N-doped carbonaceous layer enwrapping the Co@TiO_xN_y framework. Such N-doped carbon layer is introduced mainly to improve the ORR activity of the composite [9] rather than as conductive supporting material. The carbon layer also provides further confinement for ultrafine Co metal catalyst on TiO_xN_y (Figure 1b), which will be discussed later. The crystal components of Co@TiO_xN_y were identified as metallic Co, TiO, TiN and rutile TiO_2 through XRD analysis (Figure 1c, before OER). For the sake of comparison, 3DOM composites without the addition of Co precursor or ammonolysis treatment were also developed. The resulting products were identified and referred as to 3DOM-TiON and 3DOM-Co@TiO_x (Ar), respectively (Figure S3).

Figure 1d shows the 3DOM morphology of the composite: it has macroporous pores of ~150 nm and interconnected walls, providing a strong structural support for the composite. Interestingly, the 3DOM-Co@TiO_xN_y was found featured with a IV type N_2 absorption-desorption isotherm. [10] seen in Figure S4. This indicates that, in addition to the macropores, it also contains mesopores, leading to a high Brunauer-Emmett-Teller (BET) surface area of 266 m^2 g^{-1}. Together with its 3DOM porous structure, the high surface area ensures high availability of active sites, and low mass transfer resistance within the catalyst, which are beneficial for the electrochemical performance of the catalyst. Scanning transmission electron microscopy (STEM) image of Figure 1e shows that the 3DOM interconnected walls are built by aggregated nanoparticles. High magnification electron energy-loss spectroscopy (EELS) mapping (Figure 1f) confirms these nanoparticles are TiO_xN_y with their outer surfaces homogeneously covered with Co (atomic composition of 0.79%, Table S1), thus appearing to exhibit the 'core-shell' structure (**Figure 2**a). The high resolution TEM (HRTEM) image and the corresponding FFT pattern further confirm the existence of ultrafine metallic Co phase on TiO_xN_y (Figure S5). Additionally, one can see that C element is uniformly distributed on the outermost surface layer of the Co@TiO_xN_y particles, suggesting there is a carbon layer covering the 3DOM walls. This carbon layer not only improves the conductivity of the composite, but may also act like a confining layer to restrict ultrafine Co onto TiO_xN_y, and therefore can further contribute to the stability of the 3DOM-Co@TiO_xN_y. To distinguish the contribution of carbon layer and TiO_xN_y components to the composite conductivity, the electrical conductivity of 3DOM-Co@TiO_xN_y and 3DOM-Co@TiO_x (Ar) were measured. Both of the composites have a carbon layer. However, the conductivity of 3DOM-Co@TiO_xN_y (5.11 S cm^{-1}) is one order of magnitude higher than that of 3DOM-Co@TiO_x

(Ar) (0.76S cm^{-1}), seen in Figure 2b. This shows the conductivity of the 3DOM-Co@TiO_xN composite is mainly contributed by TiO_xN_y rather than the carbon layer. All of these observations strongly support the successful synthesis of ultrafine Co on conductive TiO_xN_y.

The local chemical environment on the surface of 3DOM-Co@TiO_xN_y (before OER) was examined by XPS. Its Ti 2p spectrum was deconvoluted into three overlapping doublets (Figure 2c). The minor Ti $2p_{3/2}$ peak located at 455.2 eV can be assigned to TiN or TiO. The other two peaks centered at 456.8 eV and 458.3 eV are referred to TiON and reduced TiO_{2-x} or Ti_2O_3, respectively.[11] The Ti $2p_{3/2}$ signal at 459.1 eV associated with TiO_2 is very weak, which confirms the low oxidation state of Ti in TiO_xN_y. The Co 2p spectrum of 3DOM-Co@TiO_xN_y has a characteristic $2p_{3/2}$ peak of CoO rather than metallic Co, suggesting the ultrafine Co was mildly oxidized in the air (Figure 2d). The N 1s spectrum shows the existence of N-Ti-O (396.2 eV), N-Ti (397.2 eV) and N-C components in TiO_xN_y [12] (Figure 2e). The OVs in 3DOM-Co@TiO_xN_y was probed by the O 1s XPS spectrum (Figure 2f). The peak at 530.1 eV is associated with lattice O^{2-} from O-Ti or O-Co bond, [13] the peak at 531.6 eV represents the non-lattice (defective) O^{2-} or OH species.[14] Although the formation of OH species on the catalyst surface is possible, e.g. its exposure to the ambient atmosphere, the defective O^{2-} is consistent with the wide distribution of Ti^{2+}, Ti^{3+} and Ti^{4+} states in the Ti 2p spectrum (Figure 2c), indicative of an enrichment of OVs on the TiO_xN_y surface. The locations of OV can be distributed across both of the TiO and TiO_2 lattice of TiO_xN_y. This is because: i) TiO itself is commonly featured with high OV content (11~20%); [15] ii) TiO_2 with OV has been reported to be obtained in a low-oxygen atmosphere, [16] therefore the existence of OV in TiO and TiO_2 lattice obtained under the strong reducing atmosphere of NH_3 is inevitable. Further evidence comes from a close inspection of the shape of the O-K (O 1s→2p) and Ti-L (Ti 2p→3d) core edges of EELS spectrum of 3DOM-Co@TiO_xN_y (Figure 2g), which provides chemical and electronic information on buried atoms that are in a bulk-like environment. [17] The O-K edge fine structure has been reported sensitive to O-O ordering, and damps out as the OVs concentration increases. [18] As shown in Figure 2g, the O-K edge fine structure 'washes out' in 3DOM-Co@TiO_xN_y compared with that of 3DOM-Co@TiO_x (Ar), indicating the high OVs concentration in TiO_xN_y. This is also consistent with the distinct peak shift in Ti-L edge towards low photon energy, as OVs are electron donors. The Co-L edge signal is not apparent, supportive for the low loading of Co (0.79%) on TiO_xN_y.

The beneficial effect of OVs in SMSI within Co-TiO_xN_y was supported by DFT calculations (**Figure 3**a, Figure S6). Here, TiO_2 and TiO surface were used as representative crystals for 3DOM-Co@TiO_xN_y because they are the two main crystalline oxides in TiO_xN_y observed in our pre- and post-OER XRD analysis (Figure 1c). The Ti-N component is neglected to simplify the DFT model. This is a reasonable assumption because we only focus on the OV sites. The (110) and (100) surfaces are used to model the TiO_x oxides because they are the reported stable surfaces on rutile TiO_2, [19] and featured planes for TiO as well. The adhesion energy of tetrahedral Co_4 cluster on the OV sites of non-stoichiometric cubic TiO and rutile TiO_2 (110) surfaces are 12.13 eV and 12.98 eV, respectively, indicative of the SMSI. In addition, we found that, for (110) surface, the 3D Co_4 cluster was stable only on the non-stoichiometric surfaces, whereas distortion of the Co_4 cluster occurs on the stoichiometric (reduced) surface (Figure 3a). For instance, on the stoichiometric TiO_2 (110) surface, although it has a much higher adhesion energy (19.65 eV) than that on reduced rutile TiO_2 (110), the severe distortion of Co_4 cluster results in many Co-O bonds, suggesting that the stoichiometric TiO_2 (110) surface is not favorable for the nucleation of metallic Co. On the (100) of TiO_2 and TiO, the tetrahedral structure of Co_4 cluster is preserved, and the non-stoichiometric (reduced) TiO_2 and TiO exhibit stronger SMSI than that on stoichiometric model (Figure S6). Moreover, we found that on both of the reduced (110) and (100) surfaces, the Co tends to incorporate into the TiO_2 and TiO lattice, revealing that the OV act as sites for the Co nuclei. Thus, we can further infer that, in addition to providing a SMSI, OV sites on the reduced surfaces also act as nucleation sites for Co growth during calcination. That is, the OV sites are essential in the nucleation and stabilization of the ultrafine metals. This is also supported by the fact that surface defects acting as preferred nucleation sites for the growth of metal particles have been widely recognized. [20]

The electrocatalytic activities of the 3DOM composites were evaluated by linear sweep voltammetry (LSV) with 0.1 M KOH solution. Figure 3b shows that 3DOM-Co@TiO_xN_y delivers an ORR onset potential of 0.90 V (vs. RHE). Although its onset potential still can't catch up with that of Pt/C catalyst (0.98V), 3DOM-Co@TiO_xN_y exhibits a comparable ORR half-wave potential (0.84 V) to that of Pt/C (0.85 V). Meanwhile, it also shows much higher ORR activity than the Co-free 3DOM-TiON and N-free 3DOM-Co@TiO_x (Ar). The linearity of the K-L plot and the number of electrons (n=4.0) transferred during ORR also indicate fast kinetics throughout the potential range inspected (Figure S7 a-b). In the case of OER, 3DOM-Co@TiO_xN_y exhibits the highest activity among the 3DOM composites (Figure 3c). For example, when a current density of 10 mA cm^{-2} is generated, it has a similar OER overpotential (~385 mV) as that of commercial Ir/C, whereas the overpotential for N-free 3DOM-Co@TiO_x (Ar) (417 mV) is slightly higher. The Co-free 3DOM-TiON composite has only minor OER activity, suggesting Co is the active component for OER. The high ORR and OER activity of 3DOM-Co@TiO_xN_y was further confirmed by its Tafel plot (Figure S7 c-d). The OER activities of these as-developed catalysts normalized by the electrochemically active surface area (ECSA) also show a similar trend (Figure S8 and S9), revealing that the activity enhancement of 3DOM-Co@TiO_xN_y is due mainly to an increase in intrinsic surface specific activity of 3DOM-Co@TiO_xN_y. Note that, for comprehensive comparison, three other 3DOM composites, including oxidized 3DOM-Co_3O_4@TiO_2 (air-annealed 3DOM-Co@TiO_xN_y), Co@TiO_xN_y (in NH_3 10min) and Co@TiO_xN_y (in NH_3 1hour) were also synthesized and characterized (Figure S3 and S10). Figure S11 shows that all the three Co@TiO_xN_y composites treated by NH_3 exhibit higher catalytic activities for both ORR and OER than the oxidized Co_3O_4@TiO_2, indicating the positive effect of N present in the Co@TiO_xN_y catalysts. Moreover, despite all three catalysts having similar ORR activities, the Co@TiO_xN_y (which underwent 40min-NH_3 treatment) provides the most favorable degree of oxygen vacancies that allow for the highest OER activity.

The stability of the catalyst was examined by performing a CP test at 10mA cm^{-2}. It shows that 3DOM-Co@TiO_xN_y electrode exhibits a much more stable voltage-time curve than Ir/C under OER: its output voltage increased by 5% after 20 h operation, much lower than that of Ir/C (20%), as shown in Figure 3d. When fabricated into an air electrode in a rechargeable zinc-air battery, an open circuit voltage of ~1.47 V is achieved (Figure 3e). At 1.0 V, the battery delivers a discharge current density of 95 mA cm^{-2} (Figure 3f). Notably, at low voltages under 0.8 V, 3DOM-Co@Ti_xON_y was able to deliver a much higher current density than that of Pt/C+Ir/C catalyst mixture, confirming the enhanced mass transfer realized by its 3DOM structure. Additionally, Figure 3g shows that it reaches a peak power density of 110 mW cm^{-2} at a current density of 135 mA cm^{-2} (0.80V), higher than that of Pt/C+Ir/C catalyst mixture. The specific capacity of a primary zinc-air battery with 3DOM-Co@TiO_xN_y catalyst was found to be 697 mAh g^{-1} (Figure S12), and the corresponding energy density is 865 Wh kg^{-1}, which are comparable to previously reported work. [21] The battery stabilities using Pt/C+Ir/C and 3DOM-Co@Ti_xON_y electrodes were further examined at a current density of 20 mA cm^{-2} with each cycle being 20 min. As shown in Figure 3h, the battery using Pt/C+Ir/C electrode shows a conspicuous charge and discharge voltage decay after 30 cycles (charge-discharge voltage gap of 1.36V) despite the narrow initial voltage gap (0.9V), and the degradation continues over time. The voltage gap of the battery using 3DOM-Co@Ti_xON_y electrode increases only 10 mV (from 0.97V to 0.98V) after 900 cycles (Figure S13), representing excellent cycling stability with less than 1% energy efficiency loss under highly oxidative operating conditions. As discussed in our design strategy, the excellent activity and durability of 3DOM-Co@TiO_xN_y are attributed to ultrafine Co and its SMSI with the conductive TiO_xN_y support, respectively. Essentially, the OV in TiO_xN_y support as well as its 3DOM structure play the key role. Thus, we expect its OV and structure should be maintained during OER. To verify this argument, the morphology and composition of the 3DOM-Co@TiO_xN_y upon highly oxidative OER operating conditions (at constant potential of 1.60V vs.RHE) were examined. SEM imaging confirms the 3DOM structure of the composite remained intact after 16 hours of OER testing (Figure S14). Interestingly, the XRD pattern shows its TiON and TiO_2 crystalline disappears, exhibiting only TiO crystal patterns (Figure 1d). Common sense would dictate TiO_xN_y will be eventually oxidized into TiO_2 under OER. Here, we argue that this would be true only in the absence of active OER components. In such cases, the outer surface TiO_xN_y would be "forced" to catalyze OER reaction, and gradually oxidized into TiO_2. In fact, there is only a slight oxidation on TiO_xN_y: as shown in the Ti 2p XPS spectrum (Figure 2c, after OER), the low energy Ti $2p_{3/2}$ peak associated with TiN or TiO disappears. Meanwhile, the intensity of the TiON peak decreases and the TiO_{2-x} (or Ti_2O_3) peak predominates. There is no obvious increasement of signal at 459.1eV (corresponding to TiO_2), indicating its further oxidation is prohibited.

The mild oxidation of TiO_xN_y surface is also consistent with the decrease of the metallic N-Ti peaks (N-Ti-O and N-Ti) intensity in N 1s spectrum (Figure 2e). The oxidation might result from its inevitable involvement in catalyzing OER (Figure 3c). On the other hand, due to its high electrical conductivity, it may receive the electrons released from the active ultrafine Co during OER, and therefore suppresses its further oxidation. The vanishing of TiO_2 crystal structure in XRD is likely caused by the migration of O^{2-} from inner-core TiO_2 lattice towards the OV-rich TiO_xN_y outer surface, as a consequence of the applied positive voltage in OER.

In semiconductor physics, such voltage-driven O^{2-} transportation in defective TiO_2 is well-known for resulting to its resistive switching property. [22] Figure 2d shows that the outer CoO surface of the ultrafine Co nanoparticles were oxidized into Co_3O_4 during OER, indicating Co_3O_4 is the actual catalytic phase for OER. As indicated in the O1s XPS spectrum, after OER reaction, there is a significant increase in the relative intensity of vacancy O^{2-} and O-C peaks (Figure 2f). The latter confirms the oxidation of carbon layer during OER, whereas the increased intensity of O^{2-} vacancies might have resulted from the positive voltage-induced O^{2-} migration by extracting O^{2-} from the lattice. [23] Therefore, we conclude that, despite the slight oxidation of the TiO_xN_y surface and carbon layer in the composite, its conductive and OV-rich TiO_{2-x} (or Ti_2O_3) outer surface was preserved during OER. This is the underlying key factor that contributes to the high activity and stability of the composite. Additionally, we found that the chemical state of Co@TiO_xN_y remains almost the same after ORR (Figure S15), confirming that the stability of ORR/OER bifunctional catalyst is mainly affected by OER rather than ORR.

In summary, building on our improved understanding of OVs in semiconductor physics and its resulting SMSI in solid-gas catalysis, we proposed and demonstrated a rational catalyst design strategy of synthesizing 3DOM-TiO_xN_y semiconductor supported ultrafine Co as efficient and durable electrocatalyst. Benefiting from the OVs-granted features of TiO_xN_y support, including high conductivity, oxidation-resistance, SMSI stabilizing ultrafine Co, the 3DOM-Co@TiO_xN_y composite exhibited comparable ORR-OER performance, but much longer cycling stability than noble-metals in a rechargeable zinc-air battery: it achieved over 900 charge-discharge cycles (300 hours) at 20 mA cm^{-2}. Moreover, we found that the composite undergoes a composition transition during OER. Such transition helps us elucidate the excellent stability of the composite, which is attributed to the sustained OVs and relative low oxidation state of TiO_xN_y surface during OER reaction. The strategy presented in this study can serve as a fundamental basis for selecting and designing high-performance catalyst support materials for oxygen electrocatalysis in rechargeable zinc-air batteries.

Supporting Information
Supporting Information is available from the Wiley Online Library or from the author.

Acknowledgment
The authors acknowledge the financial support from the Natural Science and Engineering Research Council of Canada (NSERC) and the 111 Project (Grant No. D17007), Henan Center for Outstanding Overseas Scientists (Grant No. GZS2018003). Thank Dr. Carmen Andrei and Dr. Andreas Korinek for TEM imaging at the Canadian Center for Electron Microscopy (CCEM) at McMaster University. Part of TEM work was performed at the Center for Functional Nanomaterials, Brookhaven National Laboratory, which is supported by the U.S. Department of Energy (DOE), Office of Basic Energy Science, under Contract No. DE-SC0012704.

Received: ((will be filled in by the editorial staff))
Revised: ((will be filled in by the editorial staff))
Published online: ((will be filled in by the editorial staff))

References

[1] a) J. Wang, W. Cui, Q. Liu, Z. Xing, A. M. Asiri, X. Sun, *Adv. Mater.* **2016**, *28*, 215; b) Y. Li, M. Gong, Y. Liang, J. Feng, J. E. Kim, H. Wang, G. Hong, B. Zhang, H. Dai, *Nat. Commun.* **2013**, *4*, 1805; c) S. Dresp, F. Luo, R. Schmack, S. Ku¨hl, M. Gliech, P. Strasser, *Energy Environ. Sci.* **2016**, *9*, 2020; d) Z. Zhao, Z. Xia, *ACS Catal.* **2016**, *6*, 1553; e) Y. P. Zhu, C. Guo, Y. Zheng, S.Z. Qiao, *Acc. Chem. Res.* **2017**, *50*, 915; f) G.L. Chai, K. Qiu, M. Qiao, M.M. Titirici, C. Shang, Z. Guo, *Energy Environ. Sci.* **2017**, *10*, 1186; g) G. A. Ferrero, K. Preuss, A. Marinovic, A. B. Jorge, N. Mansor, D. J. L. Brett, A.B. Fuertes, M. Sevilla, M.M. Titirici, *ACS Nano* **2016**, *10*, 5922; h) B. Y. Xia, Y. Yan, N. Li, H. B. Wu, X.W. Lou, X.Wang, *Nat. Energy **2016***, *1*, 15006; i) Z.-F. Huang, J. Wang, Y. Peng, C.-Y. Jung, A. Fisher, Xin Wang, *Adv. Energy Mater.* **2017**, *7*, 1700544.

[2] a) F.S. Saleh, E. B. Easton, *J. Electrochem. Soc.* **2012**, *159*, B546; b) C. Spçri, J. T. H. Kwan, A. Bonakdarpour, D. P. Wilkinson, P. Strasser, *Angew. Chem. Int. Ed.* **2017**, *56*, 5994.

[3] a) N. G. Akalework, C. J. Pan, W. N. Su, J. Rick, M. C. Tsai, J. F. Lee, J. M. Lin, L. D.

Tsai, B. J. Hwang, *J. Mater. Chem.* **2012**, *22*, 20977; b) G. Zhao, R. Mo, B. Wang, L. Zhang, K. Sun, *Chem. Mater.* **2014**, *26*, 2551; c) A. Lewera, L. Timperman, A. Roguska, N. Alonso-Vante, *J. Phys. Chem. C* **2011**, *115*, 20153.

[4] a) A. Vesel, M. Mozetic, J. Kovac, A. Zalar, *Appl. Surf. Sci.* **2006**, *253*, 2941; b) B. Avasarala, P. Haldar, *Electrochim. Acta* **2010**, *55*, 9024; c) B. Avasarala, P. Haldar, *Int. J. Hydrog. Energy* **2011**, *36*, 3965.

[5] a) A. Grimaud, K. J. May, C. E. Carlton, Y-L. Lee, M. Risch, W. T. Hong, J. Zhou, Y. Shao-Horn, *Nat. Commun.* **2013**, *4*, 2439; b) B. J. Kim, D. F. Abbott, X. Cheng, E. Fabbri, M. Nachtegaal, F. Bozza, I. E. Castelli, D. Lebedev, R. Schäublin, C. Copéret, T. Graule, N. Marzari, T. J. Schmidt, *ACS Catal.* **2017**, *7*, 3245; c) Y. Zhu, W. Zhou, Y. Zhong, Y. Bu, X. Chen, Q. Zhong, M. Liu, Z. Shao, *Adv. Energy Mater.* **2017**, *7*, 1602122.

[6] a) H. Liu, F. Zeng, Y. Lin, G. Wang, F. Pan, *Appl. Phys. Lett.* **2013**, *102*, 181908; b) X. L. Wang, C. Y. Luan, Q. Shao, A. Pruna, C. W. Leung, R. Lortz, J. A. Zapien, A. Ruotolo, *Appl. Phys. Lett.* **2013**, *102*, 102112.

[7] a) J. A. Farmer, C. T. Campbell, *Science*, **2010**, *329*, 933; b) P. Chen, A. Khetan, F. Yang, V. Migunov, P. Weide, S. P. Stürmer, P. Guo, K. Kähler, W. Xia, J. Mayer, H. Pitsch, U. Simon, M. Muhler, *ACS Catal.* **2017**, *7*, 1197; c) J. C. Matsubu, S. Zhang, L. DeRita, N. S. Marinkovic, J. G. Chen, G. W. Graham, X. Pan, P. Christopher, *Nat. Chem.* **2017**, *9*, 120; d) M-C. Tsai, T-T. Nguyen, N. G. Akalework, C-J. Pan, J. Rick, Y-F. Liao, W-N. Su, B-J. Hwang, *ACS Catal.* **2016**, *6*, 6551; e) I. N. Remediakis, N. Lopez, J. K. Nørskov, *Angew. Chem. Int. Ed.* **2005**, *44*, 1824; f) H-S. Oh, H. N. Nong, T. Reier, A. Bergmann, M. Gliech, J. F. de Araújo, E. Willinger, R. Schlögl, D. Teschner, P. Strasser, *J. Am. Chem. Soc.* **2016**, *138*, 12552.

[8] a) D. Yan, Y. Li, J. Huo, R. Chen, L. Dai, S. Wang, *Adv. Mater.* **2017**, *29*, 1606459; b) Y. Guo, Y. Tong, P. Chen, K. Xu, J. Zhao, Y. Lin, W. Chu, Z. Peng, C. Wu, Y. Xie, *Adv. Mater.* **2015**, *27*, 5989.

[9] a) N. Muthuswamy, M. E. M. Buan, J. C. Walmsley, M. Rønning, *Catal. Today.* **2018**, *301*, 11; b) H. T. Chung, D. A. Cullen, D. Higgins, B. T. Sneed, E. F. Holby, K. L. More, P. Zelenay, *Science* **2017**, *357*, 479.

[10] J. C. Groen, L.A.A. Peffer, J. Pérez-Ramírez, *Microporous Mesoporous Mater.* **2003**, *60*, 1.

[11] a) R. L. Kurtz, V. E. Henrich, *Surf. Sci. Spectra.* **1998**, *5*, 179; b) B. Avasarala, P. Haldar, *Int. J. Hydrogen Energy* **2011**, *36*, 3965.

[12] a) Q. Zuo, G. Cheng, W. Luo, *Dalton Trans.* **2017**, *46*, 9344; b) H. Jin, J. Li, F. Chen, L. Gao, H. Zhang, D. Liu, Q. Liu, *Electrochim. Acta* **2016**, *222*, 438.

[13] a) P.O. Larsson, A. Andersson, L. R. Wallenberg, B. Svensson, *J. Catal.* **1996**, *163*, 279; b) B.J. Tan, K.J. Klabunde, P.M.A. Sherwood, *J. Am. Chem. Soc.* **1991**, *113*, 855.

[14] B. Bharti, S. Kumar, H-N. Lee, R. Kumar, *Sci. Rep.* **2016**, *6*, 32355.

[15] M. D. Banus, T. B. Reed, A. J. Strauss, *Phys. Rev. B*, **1972**, *5*, 2775.

[16] a) H. Liu, F. Zeng, Y. Lin, G. Wang, F. Pan, *Appl. Phys. Lett.* **2013**, *102*, 181908; b) X. L. Wang, C. Y. Luan, Q. Shao, A. Pruna, C. W. Leung, R. Lortz, J. A. Zapien, A. Ruotolo, *Appl. Phys. Lett.* **2013**, *102*, 102112.

[17] U.vKaiser, D. A. Muller, J. Grazul, A. Chuvulin, M. Kawasaki, *Nat. Mater.* **2002**, *1*, 102.

[18] D. A. Muller, N. Nakagawa, A. Ohtomo, J. L. Grazul, H. Y. Hwang, *Nature* **2004**, *430*, 657.

[19] T. Zheng, C. Wu, M. Chen, Y. Zhang, P. T. Cummings, *J. Chem. Phys.* **2016**, *145*, 044702.

[20] a) Poppa, H. Catal. *Rev. Sci. Eng.* **1993**, *35*, 359; b) M. Che, Z. X. Cheng, C. Louis, *J. Am. Chem. Soc.* **1995**, *117*, 2008.

[21] a) X. Liu, M. Park, M. Kim, S. Gupta, G. Wu, J. Cho. *Angew. Chem. Int. Ed.* **2015**, *54*, 9654. b) C. Tang, B. Wang, H. F. Wang, Q. Zhang, *Adv. Mater.* **2017**, *29*, 1703185; c) M. Prabu, K. Ketpang, S. Shanmugam, *Nanoscale* **2014**, *6*, 3173.

[22] N. Ghenzi, M. J. Rozenberg, R. Llopis, P. Levy, L. E. Hueso, P. Stoliar, *Appl. Phys. Lett.* **2015**, *106*, 123509.

[23] Y. Du, A. Kumar, H. Pan, K. Zeng, S. Wang, P. Yang, A.T. S. Wee, *AIP Adv.* **2013**, *3*, 082107.

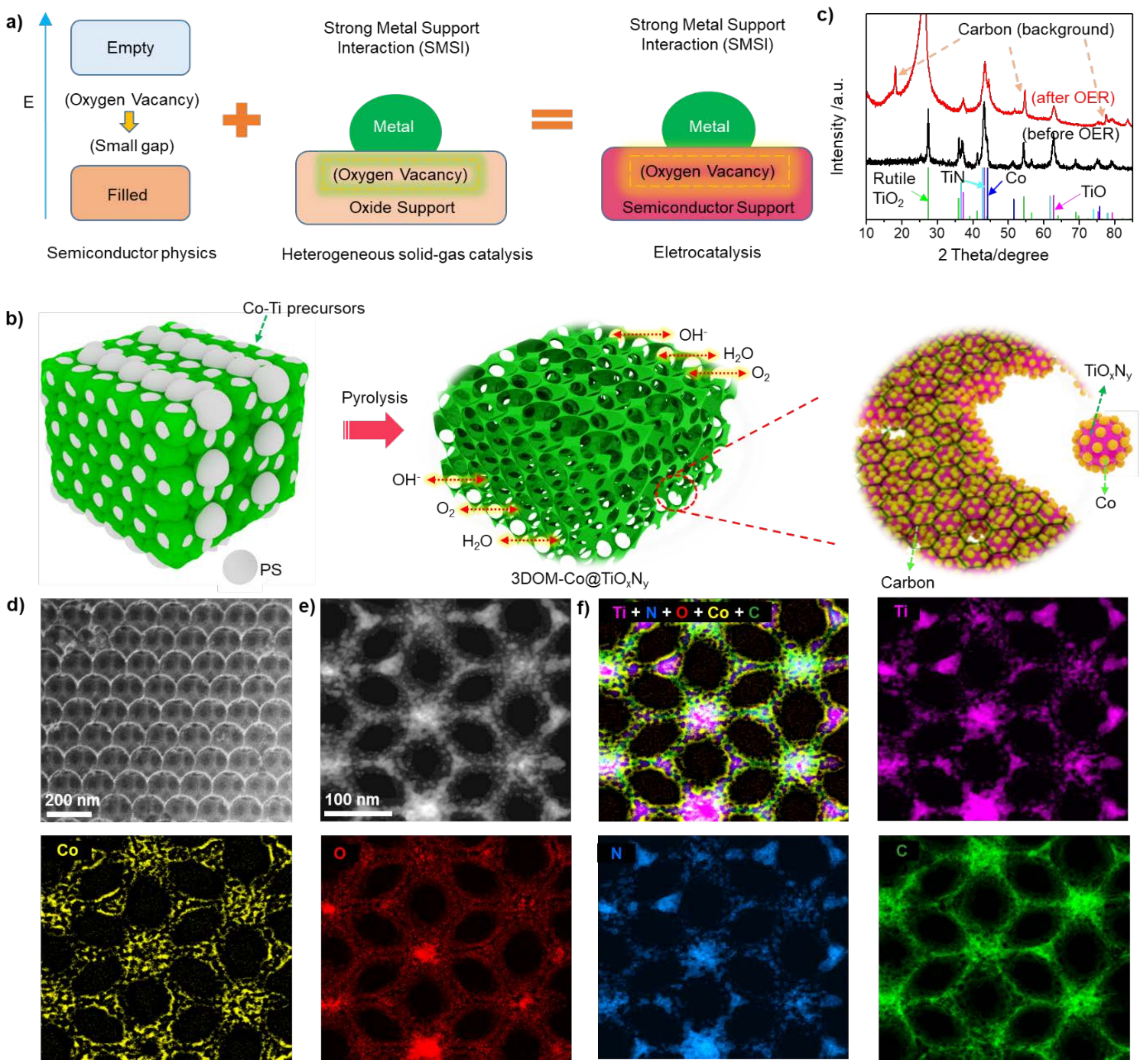

Figure 1: a) The designing strategy for semiconductor-supported metal as electrocatalysts; b) Schematic of preparation procedure for 3DOM-Co@TiO_xN_y catalyst, and the Co interface-confinement effect induced by SMSI and carbon layer; c) XRD patterns of 3DOM-Co@TiO_xN_y before and after OER reaction; d) SEM; e) STEM image and f) STEM-Electron energy-loss spectroscopy (STEM-EELS) elemental mapping (Ti, Co, O, N, and C) of 3DOM-Co@TiO_xN_y.

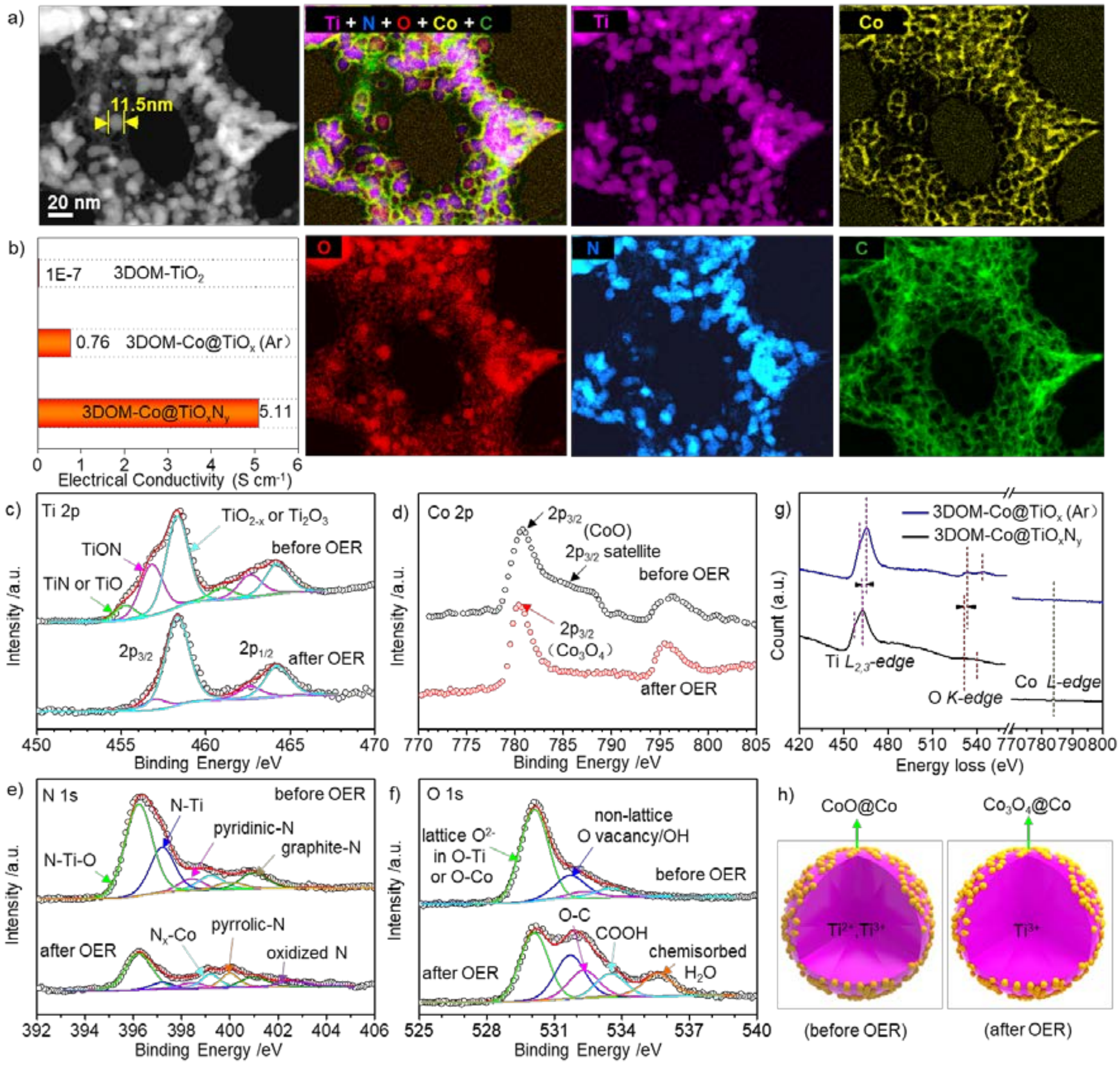

Figure 2. a) STEM image and high magnification STEM-EELS mapping of Ti, Co, O, N, and C elements; b) Electrical conductivity; c) Ti 2p; d) Co 2p; e) N1s; and f) O1s XPS spectrum of 3DOM-Co@TiO_xN_y before and after 16 hours of OER half-cell test at constant potential of 1.60V vs. RHE; g) Comparison of EELS spectra of Ti-L, O-K and Co-L core edges acquired from the as-prepared 3DOM composites; h) Schematic showing the changes of Ti 2p and Co 2p state before and after 16 hours of OER reaction.

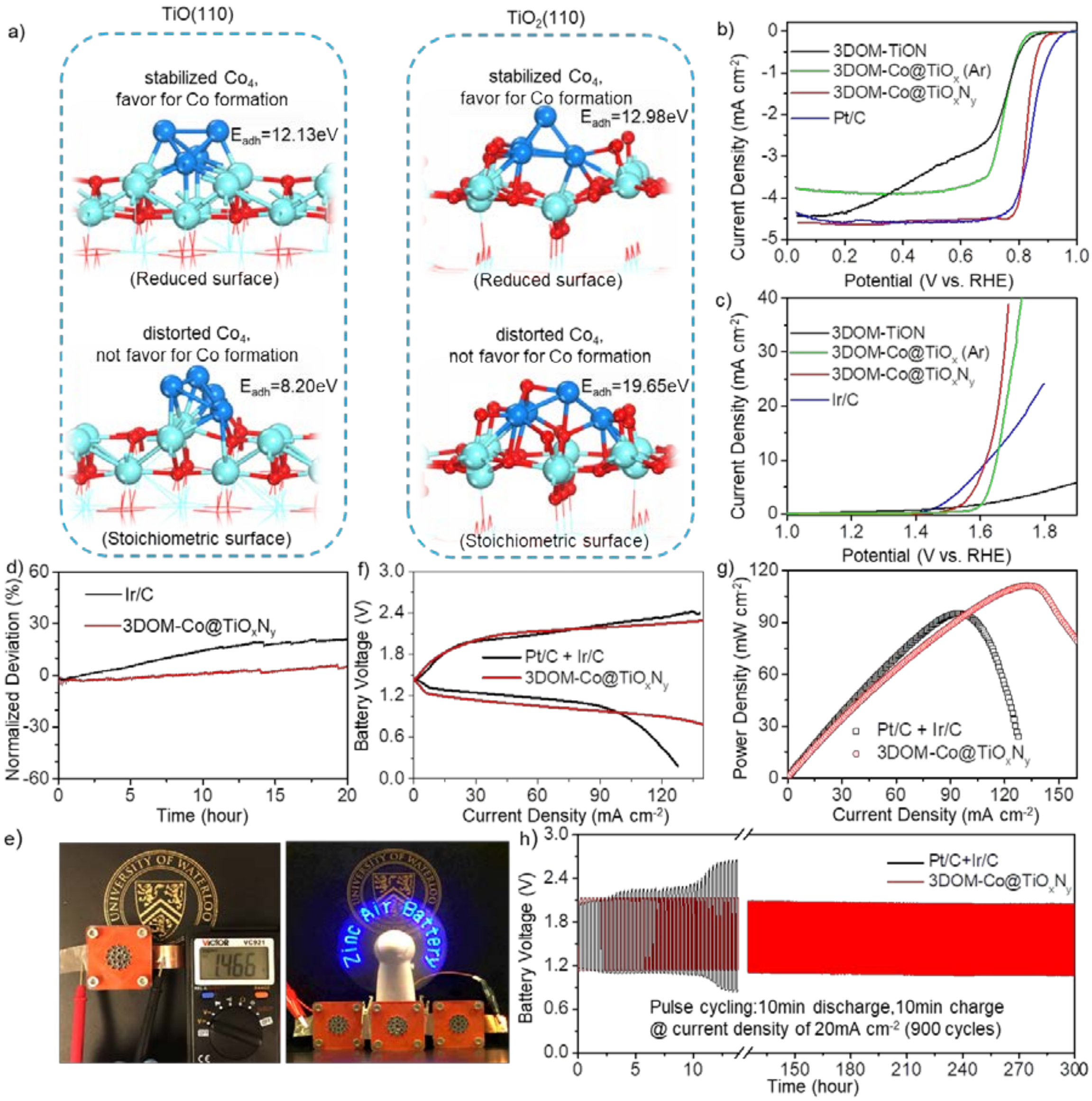

Figure 3. a) The most stable geometries and the corresponding adhesion energy of Co_4 cluster on reduced and stoichiometric TiO and TiO_2 (110) surface: blue (Co), cyan (Ti), red (O); b) ORR and c) OER LSV curves of various 3DOM composites obtained at a scan rate of 10 mV s^{-1} in 0.1 M KOH electrolyte at 900 r.p.m and 1600 r.p.m, respectively; d) Long-term OER electrolysis stability under constant current density at 10 mA cm^{-2}; e) Demonstration of the zinc-air battery configuration; f) Charge and discharge polarization curves; g) Power density plots; and h) Cycling performance of zinc-air batteries assembled using 3DOM-Co@TiO_xN_y and Pt/C+Ir/C as air electrodes in ambient air.

Oxygen vacancies (OVs)-rich semiconductor was introduced to design efficient and durable non-precious bifunctional oxygen electrocatalyst in alkaline conditions. The OVs promote the electrical conductivity of oxide support, and at the same time offers a strong metal-support interaction, which gives small metal size, high catalytic activity, and stability. It was demonstrated by synthesizing ultrafine Co metal decorated three-dimensionally ordered macroporous titanium oxynitride.

Keyword: oxygen vacancy; metal-support interaction; oxygen evolution reaction; bifunctional catalyst; zinc-air battery

G. Liu, Dr. J. Li, Dr. J. Fu, Dr. G. Jiang, G. Lui, D. Luo, Y-P. Deng, J. Zhang, Z. P. Cano, Prof. A.Yu, Dr. D. Su, Prof. Z. Bai*, Prof. L. Yang and Prof. Z. Chen*

Oxygen Vacancy-rich Semiconductor Supported Bifunctional Catalyst for Efficient and Stable Zinc-Air Battery